Applied Catalysis B: Environmental 221 (2018) 77–85

Contents lists available at ScienceDirect

Applied Catalysis B: Environmental

journal homepage: www.elsevier.com/locate/apcatb

Research Paper

Towards enhancing photocatalytic hydrogen generation: Which is more important, alloy synergistic effect or plasmonic effect?

Zhenhe Xu[a,b], Md Golam Kibria[c], Bandar AlOtaibi[c], Paul N. Duchesne[d], Lucas V. Besteiro[e], Yu Gao[b], Qingzhe Zhang[a], Zetian Mi[c,g], Peng Zhang[d], Alexander O. Govorov[e], Liqiang Mai[f], Mohamed Chaker[a], Dongling Ma[a,*]

[a] Institut National de la Recherche Scientifique (INRS), Centre Énergie, Materiaux et Télécommunications, Université du Québec, 1650 Boulevard Lionel-Boulet, Varennes, Québec J3X 1S2, Canada
[b] The Key Laboratory of Inorganic Molecule-Based Chemistry of Liaoning Province, College of Applied Chemistry, Shenyang University of Chemical Technology, Shenyang, 110142, China
[c] Department of Electrical and Computer Engineering, McGill University, 3480 University Street, Montreal, Québec, H3A 0E9, Canada
[d] Department of Chemistry, Dalhousie University, Halifax, NS, B3H 4R2, Canada
[e] Department of Physics and Astronomy, Ohio University, Athens, OH 45701, USA
[f] State Key Laboratory of Advanced Technology for Materials Synthesis and Processing, Wuhan University of Technology, Wuhan, 430070, China
[g] Department of Electrical Engineering and Computer Science, University of Michigan, Ann Arbor, MI 48109, USA

ARTICLE INFO

Keywords:
Alloys
Composite materials
Photocatalysis
Polymeric materials
Surface plasmon resonance

ABSTRACT

Synergistic effect in alloys and plasmonic effect have both been explored for increasing the efficiency of water splitting. In depth understanding and comparison of their respective contributions in certain promising systems is highly desired for catalyst development, yet rarely investigated so far. We report herein our thorough investigations on a series of highly interesting nanocomposites composed of Pt, Au and C_3N_4 nanocomponents, which are designed to benefit from both synergistic and plasmonic effects. Detailed analyses led to an important conclusion that the contribution from the synergistic effect was at least 3.5 times that from the plasmonic effect in the best performing sample, $Pt_{50}Au_{50}$ alloy decorated C_3N_4. It showed remarkable turnover frequency of > 1.6 mmol h^{-1} g^{-1} at room temperature. Our work provides physical insights for catalyst development by rationally designing samples to compare long-known synergistic effect with recently emerging, attractive plasmonic effect and represents the first case study in the field.

1. Introduction

Energy and environmental issues represent two of the greatest challenges facing humanity in this century [1–3]. Despite tremendous efforts to develop renewable energy sources, the majority of energy used so far is still derived from non-renewable fossil fuels [4–7]. One attractive solution to this problem is solar water splitting with semiconductor photocatalysts that leads to the generation of clean fuel of hydrogen [8–12]. During the past few decades, a great deal of research has been focused on the development of more efficient photocatalytic systems and deeper understanding of relevant photocatalytic mechanisms. This technology, however, still suffers from low efficiency, poor stability, and/or high production cost. For example, a state-of-the-art photocatalyst was recently reported to show an overall solar-to-hydrogen conversion efficiency of 2.0% and robust stability for at least 200 days during recycled utilization [13]. Much needs to be done, in particular, to improve the water splitting efficiency of photocatalysts. To achieve more satisfactory photocatalytic performance, alloy catalysts have attracted great attention recently. The synergetic effect between different actives sites in an alloy catalyst can possibly endow the catalyst with much improved catalytic properties [14]. For example, Ye et al. reported the enhancement in visible-light photocatalytic H_2 production through Au–Cu alloy strategy, and revealed that the synergetic effect has an important influence on water splitting [15].

A recently emerging approach for enhancing photocatalysis is to use the plasmonic effect in metal nanoparticles (NPs). Surface plasmon resonance (SPR) arises from the collective oscillation of free electrons in plasmonic structures and is characterized by strong light absorption and/or scattering, as well as the generation of intense electric fields near the metal surface [16,17]. All these characteristics may be exploited for enhancing water splitting [18,19]. Basically, there are three major underlying mechanisms for plasmon-enhanced

* Corresponding author.
E-mail address: ma@emt.inrs.ca (D. Ma).

http://dx.doi.org/10.1016/j.apcatb.2017.08.085
Received 21 June 2017; Received in revised form 23 August 2017; Accepted 24 August 2017
Available online 01 September 2017
0926-3373/ © 2017 Elsevier B.V. All rights reserved.

photocatalysis: (i) SPR induced hot electron transfer from the metal to semiconductor, (ii) enhancement in the local electromagnetic field and thus increased electron-hole pair generation rates in the semiconductor, and (iii) enhancement in scattering and thus the increase of the average photon path length in the system [18–23]. For example, Moskovits et al. reported an efficient, autonomous plasmon-enhanced whole water splitting system based on Au nanorod arrays [24]. The H_2 production rate was 5×10^{13} H_2 molecules cm^{-2} s^{-1} under 1 sun irradiation (AM 1.5G), thanks to SPR induced energetic charge carriers in Au nanorods. Although a lot of studies have clearly demonstrated that SPR can enhance photocatalytic reactions, the overall efficiencies are not satisfactory. Better understanding of mechanisms and accordingly rational system design are needed for further improvements. A general understanding is that, both electron and energy transfer between plasmonic NPs and semiconductor catalysts, important for gaining benefits from plasmonic effects in photocatalysis, can be more efficient at a shorter distance [25,26]. Specifically for hot electron transfer, the intimate contact between plasmonic nanostructures and semiconductor catalysts is highly desired. So ideally, ligand-free plasmonic metal surface is preferred for maximizing plasmon-enhanced photocatalysis with all other conditions being the same [21,27,28]. Furthermore, excited plasmonic NPs themselves can participate catalytic reactions directly. For instance, holes remained in plasmonic NPs following hot electron transfer can be directly used in and contribute to catalytic photodegradation of organic molecules [29]. In this regard, ligand-free plasmonic NPs are also preferred. Nonetheless, organic ligands are usually required to control NPs growth and prevent their coalescence in common wet chemical methods, which can obstruct the accessibility of reactants to the surface active sites of NPs, resulting in a decrease of their catalytic activity [30]. From this point of view, pulsed laser ablation in liquid (PLAL) appears as an interesting approach to yield "bare" NPs [31,32]. As demonstrated in our recent work, in addition to yielding much higher catalytic activities than chemically prepared ones, monodisperse Au NPs synthesized through a PLAL approach further feature the easy formation of intimately contacted NPs/semiconductor composites without using any linker molecules and thus ensures efficient hot electron transfer [20,33,34]. On the other hand, Pt_xAu_{100-x} (in this particular case, x = 50; at%) alloy NPs prepared via the similar method demonstrated significantly enhanced catalytic activity by a factor of 3–4 compared to pure Pt and Au NPs in nitrophenol reduction, suggesting a very strong synergistic effect in this alloy structure [35]. This exciting result motivated us to further explore if light is involved to excite SPR in catalytic reactions, whether the plasmonic effect will override the already quite impressive synergistic effect. It is worthwhile to point out that although both the plasmonic effect and the synergistic effect in alloys have been separately studied, their in depth comparison has rarely been reported. Moreover, in many cases, both effects can co-exist and entangle in a single system. It is indeed not trivial to disentangle enhancement mechanisms and identify the dominant one in a complex system. Such knowledge, however, can be extremely helpful for future catalysts development.

Herein, we intended to answer a fundamentally and technologically important question: for enhancing photocatalytic hydrogen generation, which approach is more effective, by exploring the synergistic effect in alloys or by using the plasmonic effect? We based our investigation on a very promising catalytic system containing carbon nitride (C_3N_4), Pt, Au, and Pt_xAu_{100-x} (x = 0, 30, 50, 70, 100 at.%) NPs with a "bare and clean" surface were fabricated by the PLAL in pure water and studied in detail using X-ray absorption spectroscopy with synchrotron irradiation in order to understand the alloy structure and build up a structural model at the atomic level. Then, we used these NPs to decorate C_3N_4 and the formation process is shown in Scheme 1. The hydrogen generation activity of the C_3N_4 supported Pt_xAu_{100-x} alloy NP catalysts (denoted as Pt_xAu_{100-x}/C_3N_4) was assessed and compared with C_3N_4 supported monometallic Pt and Au NPs, and their mixtures (denoted as Pt/C_3N_4, Au/C_3N_4, and Pt + Au/C_3N_4, respectively). We observed that $Pt_{50}Au_{50}/C_3N_4$ sample exhibited the best hydrogen generation ability under visible light, even though mixed Pt + Au/C_3N_4 samples exhibited much stronger plasmon absorption in the visible region. The turnover frequency (TOF) of this sample reached as high as 1.6025 mmol h^{-1} g^{-1} at room temperature. Further by doing electrochemical and wavelength-resolved measurements and theoretical calculations, relevant mechanisms are discussed and a key role of the synergistic effect in the alloy NPs was identified and highlighted. In addition to achieving impressive TOF for H_2 generation, this work represents the first systematic investigation and comparison of the synergistic and plasmonic effects in samples expected to benefit from both.

2. Experimental

2.1. Preparation of targets for laser ablation

Different ratios of Pt and Au micropowders (Pt_xAu_{100-x}, x = 100, 70, 50, 30, 0) were mechanically mixed for 0.5 h and then compression molded [35]. Typically, 0.5 g of Pt-Au powder mixtures at different ratios were placed into a steel die with a diameter of 8 mm and pressed with a total pressure of 12 tons to form a compact pellet using a CARVER Press for 20 min. All the operations were performed at room temperature. The pellet has a thickness of 1.5 mm and a diameter of 8 mm. They were used for laser ablation.

2.2. Synthesis of NP colloids by laser ablation

Laser ablation was carried out with a KrF excimer laser (GSI Lumonics PM-846, wavelength: 248 nm; exciting voltage: 37 kV; pulse duration: 17 ns; repetition rate: 20 Hz). The laser beam was focused using an objective lens, with a focal length of 7.5 cm, onto the pellet target. The target was placed at the bottom of a 5 mL baker filled with pure water. The depth of the solution layer above the target was ~10 mm. The lens-to-target distance was fixed in order to guarantee the consistency of the ablation spot size (~0.4 mm × 0.5 mm) on the target. The laser fluence on the target was set at ~40.0 J cm^{-2}. The actual amounts of Pt and Au in all the samples were determined by Neutron activation analysis method.

2.3. Synthesis of C_3N_4

Typically, 30 g of urea was placed into an alumina crucible with a cover, and then the crucible was heated in a muffle furnace at 250 °C for 1 h, 350 °C for 2 h and 550 °C for 2 h with a heating rate of 2 °C min^{-1}. The yielded yellow powder was washed with nitric acid (0.1 mol L^{-1}) and distilled water to remove any residual alkaline species (e.g. ammonia) adsorbed on the surface of the product, and then the product was dried at 80 °C for 12 h.

2.4. Synthesis of NP/C_3N_4 catalysts

To 40 mg of C_3N_4, different volumes of freshly prepared Pt_xAu_{100-x} (x = 100, 70, 50, 30, 0) NP solution were added and mixed by shaking. Then, a few drops of HCl aqueous solution (0.1 mol L^{-1}) was added to the above soution and the pH value was about 5. The mixture solution was incubated at room temperature for ~30 min to assemble metal NPs onto the surface of C_3N_4. After centrifugation, a solid product precipitated and supernatant became clear and completely colorless, indicating that all the metal NPs were efficiently loaded onto C_3N_4. We were able to modulate the loading of Pt, Au and alloy NPs on the surface of C_3N_4 using various volumes of freshly prepared NP solutions and further confirm their content using neutron activation analysis (NAA).

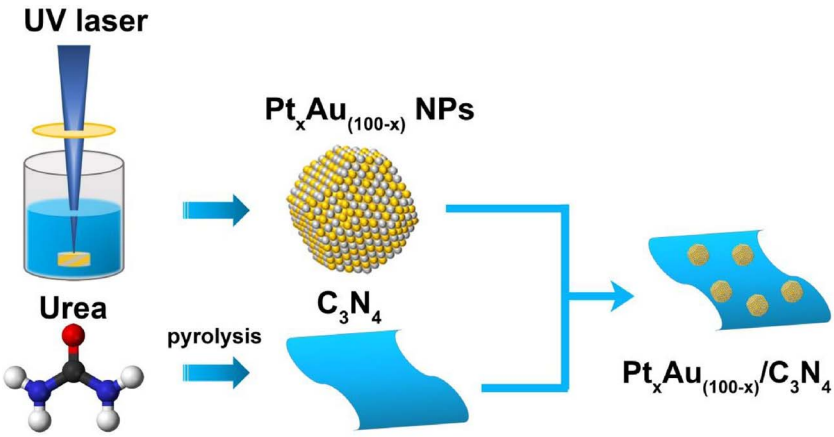

Scheme 1. Schematic illustration of the preparation process of Pt_xAu_{100-x} (x = 100, 70, 50, 30, 0)/C_3N_4.

2.5. Characterization

Powder X-ray diffraction (XRD) of Pt_xAu_{100-x} NPs was performed on a Philips X'pert diffractometer using a Cu Kα radiation source (λ = 0.154 nm). A UV–vis (UV-vis) spectrometer (Varian 5000) was used to measure the absorption spectra of Pt_xAu_{100-x} NP solutions in quartz semi-microcuvettes (light path: 10 mm) in the transmission mode at room temperature. All spectra were collected over the wavelength range of 300–750 nm with a scan speed of 600 nm min^{-1}, and background absorption by water was subtracted. The crystal structure of other samples was characterized by a Bruker D8 Advanced Diffractometer, again using Cu Kα radiation. A transmission electron microscope (TEM, JEOL 2100F) was applied for the analysis of microstructure and composition. The chemical states of involved elements were studied using X-ray photoelectron spectroscopy (XPS, ESCALAB 220I-XL spectrometer) equipped with an Al Kα (1486.6 eV) monochromatic source. UV–vis-NIR absorption spectroscopy was conducted using a Varian 5000 spectrometer. NAA was performed using a SLOWPOKE nuclear reactor to quantify the concentration of Pt_xAu_{100-x} NPs in solution, as well as the content of Pt_xAu_{100-x} NPs in Pt_xAu_{100-x}/C_3N_4 composite. All experiments were carried out under ambient conditions. X-ray absorption spectroscopy (XAS) data were acquired using the BM-20 endstation (CLS@APS) of the Advanced Photon Source, located at Argonne National Laboratory, Argonne, IL. A double-crystal Si (111) mirror monochromator was used to select the incident X-ray energy and detuned to 80% to reject any higher-order harmonics. A 12-element Ge fluorescence detector was used to acquire the Pt and Au L_3-edge XANES spectra, and gas-ionization chamber detectors were used to those of the Pt and Au foil references. A Displex low-temperature sample stage was used to hold the $Pt_{50}Au_{50}$ sample at 90 K; this low-temperature method was able to increase signal intensity via suppression of thermal vibrations of atoms within the nanoparticles. Au and Pt reference foil spectra were readily acquired at ambient temperature. Processing and fitting of the XAS data was performed using WinXAS software and using theoretical scattering paths generated with FEFF8 [36,37].

2.6. Photocatalysis activity tests

The photocatalytic reaction was performed in a Pyrex chamber with a quartz lid. The reaction was performed by mixing aqueous solution of a composite photocatalyst (0.04 g) with 10 vol% triethanolamine solution as a sacrificial agent for hydrogen production. Before starting the photocatalytic reaction, the solution was purged by Ar gas for 30 min. A 300 W Xenon lamp (Cermax, PE300BUV) with different filters was used as an outer irradiation source. During testing, the solution was continuously stirred with a magnetic stirrer and the temperature of the reaction solution was controlled by a water cooling system. The chamber was then evacuated. The gases produced from the reaction were sampled using a vacuum tight syringe. A gas chromatograph (Shimadzu GC-8A) equipped with a thermal conductivity detector and high-purity Ar carrier gas was used to analyze reaction-evolved gases. The experimental error in the evolution of H_2 was estimated to be ~10%, which is ascribed to the manual sampling of the gas.

2.7. Electrochemical analysis

Working electrodes were prepared on transparent fluorine-doped tin oxide (FTO) coated glass. Briefly, 50 mg catalyst powder was mixed with 2 mL of dimethylformamide under sonication for 30 min to get slurry. The slurry was spread onto FTO glass, whose side part was protected using Scotch tape. After air drying, the electrode was heated at 300 °C for 30 min in nitrogen to improve adhesion. A copper wire was connected to the side part of the FTO glass using a conductive tape. Uncoated parts of the electrode were covered with epoxy resin in order to avoid any direct contact between the electrolyte and the conducting back-contact and/or the copper wire. Electrochemical measurements were performed in a typical three electrode cell, using a Pt wire and a Ag/AgCl electrode as the counter electrode and reference electrode, respectively. Electrolyte was a 0.5 mol L^{-1} Na_2SO_4 (pH = 6.8) aqueous solution without any additive and was purged with nitrogen for 30 min prior to measurements. Electrochemical experiments were taken on a Gamry electrochemical station (Reference 3000™). A 300 W Xe lamp was used as the light source and positioned 3 cm away from the photoelectrochemical cell. The EIS was performed with an AC voltage amplitude of 20 mV and the frequency ranged from 10 mHz to 200 KHz at a DC bias of 0.5 V vs. Ag/AgCl in a 0.5 mol L^{-1} Na_2SO_4 aqueous solution.

3. Results and discussion

Pure and alloy metal NPs were all fabricated by PLDL. Fig. 1A and B exhibit the transmission electron microscopy (TEM) images of representative $Pt_{50}Au_{50}$ NPs with an average size of ~3.5 ± 1 nm. Energy dispersive spectroscopy (EDS) analysis confirmed that the concentration of Pt in this sample was about 49.5% (inset in Fig. 1A), close to the nominal concentration of 50%. TEM and EDS of other NPs with different stoichiometric ratios of Pt-to-Au (Pt, $Pt_{70}Au_{30}$, $Pt_{30}Au_{70}$ and Au) are shown in Fig. S1-S4 (Supporting Information). Powder X-ray diffraction (XRD) shows (Fig. S5, Supporting Information) that the introduction of Au atoms into the Pt lattice can lead to peak shift toward smaller 2θ values due to the substitution of smaller Pt atoms in the fcc lattice.

Efforts were made to better understand the arrangement of Pt and Au atoms in the alloy structure at the atomic level by resorting to synchrotron technique. Due to the fact that the Pt and Au L_3 absorption

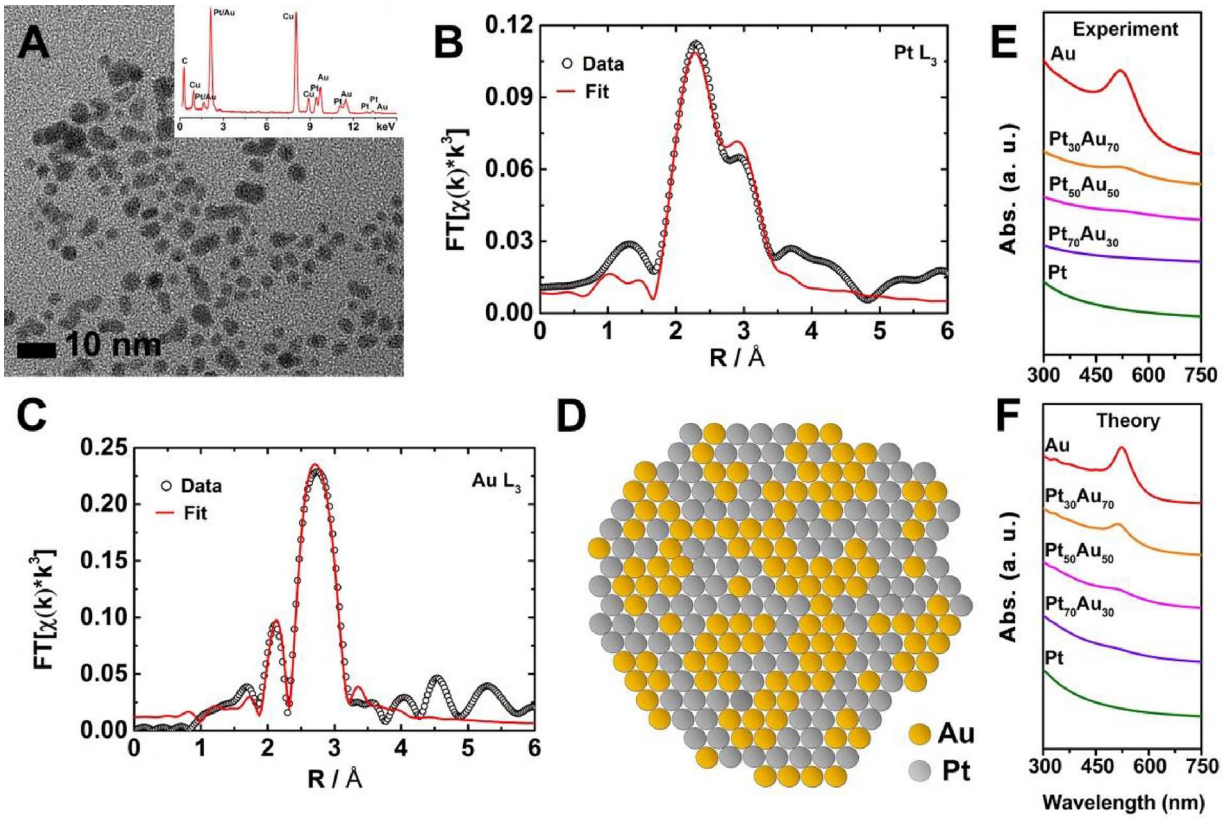

Fig. 1. (A) TEM images of $Pt_{50}Au_{50}$ NPs prepared by PLAL. The inset in (A) shows the corresponding EDX spectrum. (B, C) Fitted, Fourier-transformed Pt and Au L3 edge EXAFS spectra illustrating the good agreement between the fit and experimental data. (D) Graphical representation of the structure of the $Pt_{50}Au_{50}$ alloy NP. (E) Optical absorption spectra of Pt_xAu_{100-x} (x = 100, 70, 50, 30, 0) alloy NPs. (F) Calculated extinction spectra of Pt_xAu_{100-x} (x = 100, 70, 50 30, 0) alloy NPs.

edges correspond to 2p-to-5d electronic transitions, analysis of the X-ray absorption near edge structure (XANES) region of the corresponding X-ray absorption spectroscopy (XAS) can provide useful valence state information for these elements [29]. The XANES spectra of $Pt_{50}Au_{50}$ and the corresponding metal foils are presented in Fig. S6 (Supporting Information) for comparison. From them, basically no obvious electronic change was identified due to alloying. This, however, does not absolutely exclude the possible d-band center shift; the subtle d-band shift could simply not be resolved at such high energy measurements in the current case. In order to determine more conclusive structural information than this, the extended X-ray absorption fine structure (EXAFS) fitting method, which yields useful structural information in terms of both the number of neighboring atoms (coordination number, CN) and corresponding bond lengths for the element of interest as an alternate approach was used. EXAFS spectra were acquired by measuring the X-ray fluorescence of the $Pt_{50}Au_{50}$ sample at both the Pt and Au L_3 absorption edges. Fitted, Fourier-transformed $Pt_{50}Au_{50}$ EXAFS spectra are presented in Fig. 1B and C. Only a single metal–metal scattering path each could be included for fitting the Pt and Au data (Pt-M and Au-M, respectively); however, much structural information can still be inferred from this method. In terms of CN, the values determined for Pt-M (11 ± 2) and Au-M (11 ± 1) were both very similar and of large magnitude. This similarity indicates that neither element is predominantly distributed at either core or surface sites, confirming the formation of a uniform alloy structure, which has constant composition on the surface and in the interior. The magnitude indicates a low incidence of structural defects in the alloy NPs' structure. Perhaps more informative than these CNs are the Pt-M and Au-M bond lengths (2.772 ± 0.008 Å and 2.838 ± 0.004 Å, respectively), and their differences from those of bulk Pt–Pt (2.775 Å) and Au–Au (2.884 Å) [38]. It is well known that metal NPs tend to exhibit lattice contraction as a function of their decreased particle size, as well as due to intermetallic bonding ("Vegard's Law") [39]. In the case of $Pt_{50}Au_{50}$, a particle size of ~5 nm would suggest a lattice contraction of ~0.5 to 1%, or a decrease of approximately 0.02 Å in both the Pt-M and Au-M bond lengths. However, the Pt-M length is longer than this, and the Au-M one is shorter, which can be explained in terms of the intermetallic effect, implying a significant degree of mixing occurs in the $Pt_{50}Au_{50}$ sample between Pt and Au atoms. Based on these analyses, the structural model is proposed (Fig. 1D).

The ultraviolet (UV)-visible-near infrared (NIR) absorption spectra of Pt_xAu_{100-x} alloy NPs (Fig. 1E) show that Pt NPs did not exhibit considerable absorption in the visible wavelength range, but Au NPs showed a characteristic SPR peak at 516 nm. As the content of Pt increased in alloy NPs, plasmon resonance intensity in the visible range decreased and even became non-observable. Fig. 1F shows calculated extinction spectra of the PtAu alloy NPs within the Maxwell-Garnett model of a composite PtAu medium, along with those of pure Pt and Au NPs, based on the model in Fig. 1D. As shown in this atomistic structure model, the PtAu alloy NP is composed of clusters of Au and Pt atoms. In the optical model, we also assume clusters of the two constituting materials, Au and Pt. Then, we involve the empirical dielectric constants for Au and Pt and water or a host material for the NPs. The Maxwell-Garnett approach gives very good agreement between the calculation results and experiment (Fig. 1E and F). The plasmonic peak in the visible range gradually decreases with increasing Pt content. The spectra of pure Pt NPs do not show any plasmonic peak since platinum does not have plasmonic peaks in the visible range. Simultaneously, gold is a well-known plasmonic material and the Au NPs exhibit strong plasmonic resonance. Our calculation results reproduce the gradual decrease of the plasmonic peak as we move from Au NPs to Pt NPs. Alloy NPs are thus both catalytic and plasmonic in the visible range. The alloy NPs thus serve as an ideal platform for studying and comparing the plasmonic and synergetic effects on catalysis.

To quantitatively determine and understand the mechanistic role of above synthesized NPs in water splitting, we chose C_3N_4 as the support in the current investigation. Since Wang's pioneering work in 2009 on C_3N_4 for H_2 production under visible light [40], C_3N_4 photocatalyst has attracted numerous attention due to its relatively low band gap (E_g = 2.7 eV) and proper conduction band (CB) and valence band (VB) edges (1.8 and −0.9 eV versus hydrogen electrode (RHE)) capable of driving both H_2 and O_2 evolution reactions, which empowers it to be a promising visible-light active photocatalyst for water splitting [13]. Moreover, C_3N_4 is composed of carbon and nitrogen, both of which are abundant in the earth. Also importantly, it is stable up to 600 °C in air and chemically stable in most solvents [13]. All these characteristics make it a very promising photocatalyst for versatile applications. Yet, it exhibits a rather low photocatalytic efficiency in water splitting so far [41]. Towards improving the efficiency, scientists have adopted a lot of strategies not only to further enhance the light-absorption ability of C_3N_4-based catalysts, but also to improve the separation efficiency of charge carriers in them. For the latter, one of the most attractive approaches relies on the use of noble metals on the surface of C_3N_4 sheets to facilitate the charge separation and to lower activation barriers for H_2 or O_2 evolution as well. Herein, a selected series of metal NPs, including most popular Pt NPs, plasmonic Au NPs, and alloy NPs are investigated, which are expected to enhance light absorption via the plasmonic effect and also increase photocatalytic activity through the synergistic effect, and thereby serving as an ideal platform for studying and comparing different enhancement mechanisms of photocatalysis in depth. C_3N_4 was synthesized by thermal polymerization of urea [42], and exhibited a 2-dimensional platelet-like morphology (Fig. 2A). The chemical structure of as-prepared C_3N_4 was confirmed by performing X-ray photoelectron spectroscopy (XPS) (Fig. S7, Supporting Information) and XRD (Fig. 2G) measurements.

The metal NPs were loaded onto C_3N_4 by mixing C_3N_4 with freshly prepared metal NP solutions and the loading level was precisely controlled by various the volume of NP solutions. The microstructure of formed metal NPs/C_3N_4 (Pt/C_3N_4, $Pt_{70}Au_{30}/C_3N_4$, $Pt_{50}Au_{50}/C_3N_4$, $Pt_{30}Au_{70}/C_3N_4$, and Au/C_3N_4) samples are revealed by TEM images (Fig. 2B–F). After deposition of different kinds of metal NPs on C_3N_4, the platelet-like morphology of C_3N_4 remained intact; meanwhile, in general the metal NPs were well dispersed on the C_3N_4 surface, although at the nanoscale some areas seemed to have more NPs than others. No un-attached metal NPs were observed on TEM grids, indicating a high affinity of the laser fabricated metal NPs to C_3N_4. The XRD patterns of metal NPs/C_3N_4 samples containing different kinds of metal NPs are shown in Fig. 2G. Compared with the C_3N_4 sample, the metal NPs/C_3N_4 samples presented an additional diffraction pattern of metal NPs. For instance, the Au/C_3N_4 sample displayed a two-phase structure and showed diffractions from both C_3N_4 and Au. However, due to the quite low loading of metal NPs in all these samples, only the most prominent diffractions of metal NPs could be observed. The optical property of C_3N_4-based materials was studied by UV–vis-NIR absorption spectroscopy, and the results are shown in Fig. 2H. As expected, pure C_3N_4 showed typical absorption sharply arising from 450 nm towards shorter wavelengths, originating from the excitation of electrons in C_3N_4 from the VB populated by N2p orbitals to the CB formed by C2p orbitals [40]. After deposition of metal NPs on the surface, enhanced absorption appeared from visible extending to near-infrared, attributed to the SPR of metal NPs and their agglomerates.

Fig. 3A shows the evolution of H_2 from Pt, Au and alloy NPs/C_3N_4 samples under visible light illumination (λ ≥ 420 nm) at a constant temperature (~30 °C). The overall metal loading in all the samples for photocatalytic testing was set at 3.0 wt%, as confirmed by Neutron activation analysis (NAA) measurements. It is noted that the bare C_3N_4 exhibited the lowest overall activity for water splitting, highly likely due to the fast charge recombination in it. The H_2 generation of the Pt/C_3N_4 sample was much more efficient than that of the Au/C_3N_4 sample, indicating that herein enhanced visible light absorption does not play a key role in H_2 evolution although the latter shows strong and broad absorption in the visible range due to the Au SPR. The activity seems thus much affected by the nature of involved metal NPs, which agrees well with previous studies [43]. Since Pt provides the smallest over voltage and favorable kinetic effects in water splitting, whereas Au shows SPR, we believe that their alloy NPs with possible Pt-Au synergistic effect and hybrid plasmon effect will constitute a very interesting comparative study system and may yield even higher catalytic activity than their single components. The rational is further detailed as follows: 1) the d-band center of Pt is predicted by Density Functional Theory (DFT) to significantly shift from −2.25 eV to −1.83 eV once alloying with Au, thereby largely influencing catalysis processes [35]; 2) the alloy NPs may also show SPR, which can be beneficial for photocatalysis [19]; 3) a synergistic effect of Pt and Au components can be tuned and strengthened by adjusting the composition of the metal alloys, and thus allowing to optimize H_2 production [44]. After 120 min irradiation, the order of H_2 generation rate can be summarized as follows: $Pt_{50}Au_{50}/C_3N_4$ > $Pt_{70}Au_{30}/C_3N_4$ > $Pt_{30}Au_{70}/C_3N_4$ > Pt/C_3N_4 > Au/C_3N_4 > C_3N_4. The H_2 evolution rates of both Pt-rich ($Pt_{70}Au_{30}$)/C_3N_4 and Au-rich($Pt_{30}Au_{70}$)/C_3N_4 alloys were significantly higher, about 2.0 and 3.3 times, than those of their monometallic counterparts (i.e., Pt/C_3N_4 and Au/C_3N_4), respectively. These results immediately highlight the significance of alloying. The greatest beneficial effect of alloying was observed for the Pt-to-Au ratio of 1:1. Most notably, the H_2 evolution rate of the $Pt_{50}Au_{50}/C_3N_4$ photocatalyst could reach 64.1 μmol h^{-1}, which was about 3.0 and 5.6 times higher than that of Pt/C_3N_4 and Au/C_3N_4, respectively. In terms of TOF, $Pt_{50}Au_{50}/C_3N_4$ photocatalyst is 1.6025 mmol h^{-1} g^{-1} at room temperature. Such impressive activity could be attributed to enhanced light absorption in the visible range (in this case hot electron transfer from Au to C_3N_4 is involved) due to the plasmonic effects and/or the synergistic effect between Pt and Au arising from the change of the d-band center and kinetics. Only with these results, however, it was difficult to assess their respective contributions. One thing is certain that the synergistic effect in the alloy NPs is non-negligible and indeed very significant, since the level of light absorption enhancement is far below that of catalytic activity enhancement. Even assuming the same light absorption of Au/C_3N_4 and $Pt_{50}Au_{50}/C_3N_4$ in the visible range, the latter was several times more active. Rough estimation of light absorption difference in these two samples was further done by integrating absorption from 420 to 700 nm of Au and $Pt_{50}Au_{50}$ NPs dispersed in solution, which yielded 3.1 times stronger absorption by the former in this wavelength range; the 5.6 times higher activity of $Pt_{50}Au_{50}/C_3N_4$ thus could not be explained solely by the plasmonic effect. We further studied the stability of this highly active catalyst of $Pt_{50}Au_{50}/C_3N_4$. The experiment on its cyclic performance for H_2 production was run under visible-light illumination (λ ≥ 420 nm) at ~30 °C for 5 consecutive cycles; no obvious decay of H_2 production was observed, suggesting their quite good stability during water splitting (Fig. 3B). Briefly, these water splitting results clearly show the high potential of the alloy catalyst of $Pt_{50}Au_{50}/C_3N_4$, whose activity was enhanced from both plasmonic and synergistic effects.

To gain deeper insights into catalysis kinetics, the electrochemical behavior of C_3N_4, Pt/C_3N_4, Au/C_3N_4, and $Pt_{50}Au_{50}/C_3N_4$ was studied in the standard three-electrode cell. The transient photocurrents of the samples as a function of time were measured at 0.5 V during ON/OFF illumination cycles with a 300W xenon lamp. All of the samples exhibited prompt and reproducible photocurrent responses upon illumination (Fig. 3C). When the irradiation was turned off, the photocurrent rapidly dropped to nearly zero, and the photocurrent reverted to the original value once light was switched back on again. The transient photocurrent densities of $Pt_{50}Au_{50}/C_3N_4$, Pt/C_3N_4, Au/C_3N_4, and C_3N_4 were 12.5, 7.5, 2.5, 0.9 μA/cm^2, respectively. Note that the $Pt_{50}Au_{50}/C_3N_4$ sample exhibited the highest transient photocurrent density among the four samples tested, which was about 1.6, 5.0, 13.9 times higher than those of Pt/C_3N_4, Au/C_3N_4, and C_3N_4, respectively. The

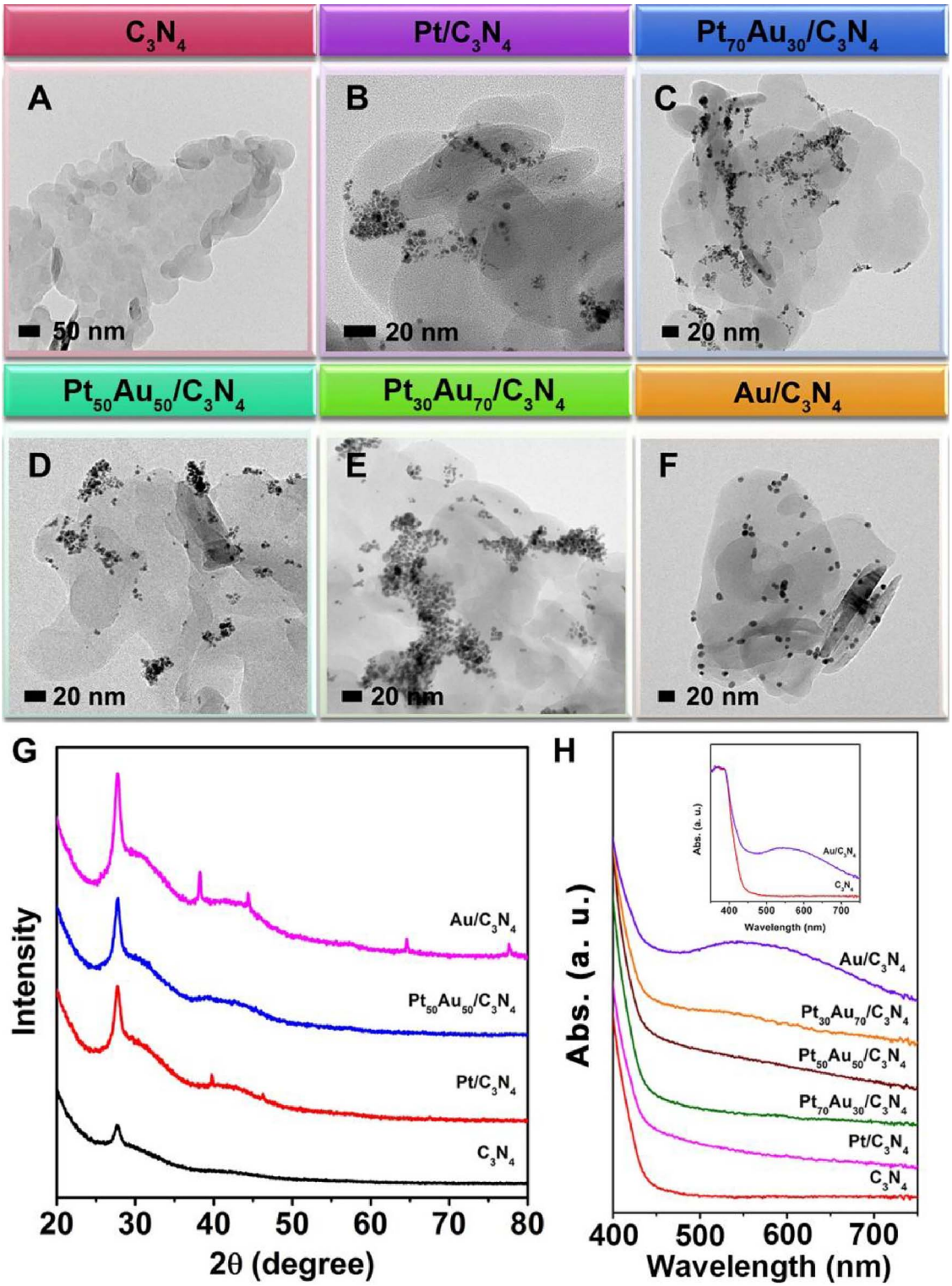

Fig. 2. TEM images of (A) C_3N_4, (B) Pt/C_3N_4, (C) $Pt_{70}Au_{30}/C_3N_4$, (D) $Pt_{50}Au_{50}/C_3N_4$, (E) $Pt_{30}Au_{70}/C_3N_4$ and (F) Au/C_3N_4. (G) XRD patterns of C_3N_4, Pt/C_3N_4, $Pt_{50}Au_{50}/C_3N_4$ and Au/C_3N_4. (H) Absorption spectra of C_3N_4 and Pt_xAu_{100-x} (x = 100, 70, 50, 30, 0) alloy NPs/C_3N_4. The inset in (H) shows the contrastive absorption spectra of C_3N_4 and Au/C_3N_4.

trend is in line with that of H_2 production described in the last section, further confirming the high promise of alloy samples. The charge transfer behavior of the above samples was further studied with electrochemical impedance spectroscopy (EIS) in dark (Fig. 3D). The radius of the semicircular Nyquist plots has long been associated with the charge transfer process at the corresponding electrode/electrolyte interface, with a smaller radius corresponding to a lower charge transfer resistance. The $Pt_{50}Au_{50}/C_3N_4$ sample exhibited the smallest radius among the above four samples, suggesting that the most efficient interface charge transfer took place in the alloy system. Since no light was involved in this experiment, no plasmonic effects were expected. These results therefore serve as direct evidence for the synergistic effect in the alloy sample, which changes underlying kinetic processes.

To further confirm the synergistic effect from alloying Pt and Au, a comparison was made with the mixture of Pt and Au NPs loaded onto C_3N_4. These samples were prepared by physically mixing appropriate

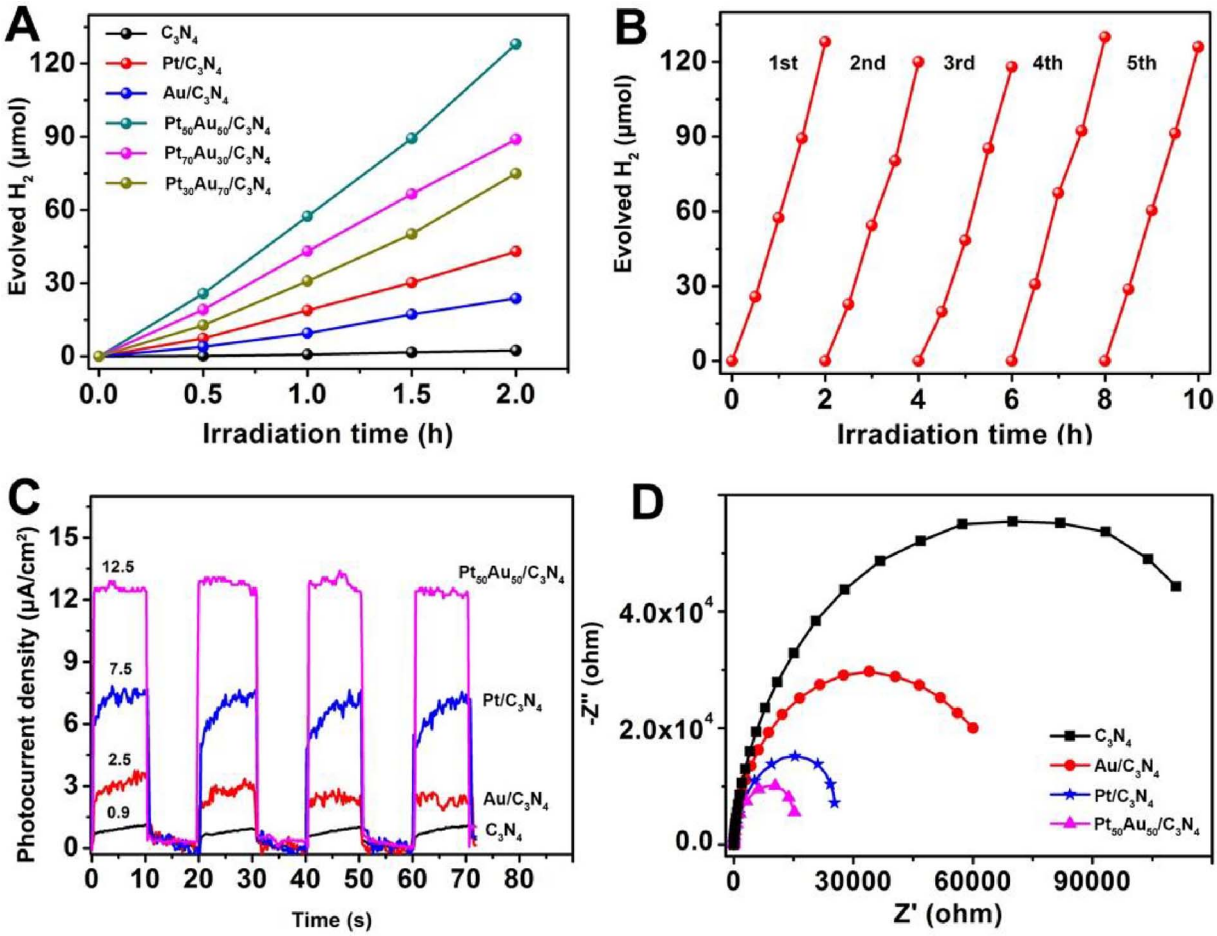

Fig. 3. (A) Photocatalytic H_2 production of C_3N_4 and Pt_xAu_{100-x} (x = 100, 70, 50, 30, 0)/C_3N_4 under visible light irradiation (λ ≥ 420 nm). (B) Stability study of $Pt_{50}Au_{50}/C_3N_4$ for H_2 evolution under visible light irradiation (λ ≥ 420 nm). (C) Photocurrent responses of C_3N_4, Au/C_3N_4, Pt/C_3N_4, and $Pt_{50}Au_{50}/C_3N_4$ electrodes at 0.2 V bias vs Ag/AgCl in a 0.2 M Na_2SO_4 electrolyte solution under Xe irradiation. (D) Nyquist plots, obtained from EIS measurements, for C_3N_4, Au/C_3N_4, Pt/C_3N_4 and $Pt_{50}Au_{50}/C_3N_4$.

amounts of Pt NPs and Au NPs at the same Pt-to-Au ratios as those in alloy samples. Two important features of the mixed Pt + Au/C_3N_4 samples make them distinctively different from alloy PtAu/C_3N_4. First, they can strongly absorb the visible light through the SPR effect of Au NPs, much stronger than corresponding alloy samples, although the intensity varies with the content of the Au NPs in the mixed samples. On the other hand, Pt and Au atoms in the mixed samples do not have as intimate contact as that in the alloy NPs. As a result, Pt-Au interactions and resulting synergistic effect are expected to be much weaker, even un-observable. As it can be seen from Fig. S8 (Supporting Information), an obvious absorption band in the visible region between 500 and 600 nm, characteristic of the SPR of the Au NPs, could be clearly observed in all the mixed samples, with Pt-to-Au ratios varying from 70:30, 50:50 and to 30:70. Fig. 4A shows the comparison of the H_2 evolution rates with respect to the Pt content in alloy Pt_xAu_{100-x}/C_3N_4 and mixed xPt + (100-x)Au/C_3N_4. Clearly, the physically mixed samples showed much lower H_2 evolution rates than alloy counterparts, even though they contained the same quantity of Au and Pt and showed strong visible absorption, which unambiguously suggests that the synergistic effect, instead of the plasmonic effect, significantly contributes to the much higher photocatalytic activities achieved in the alloy samples. Specifically, for $Pt_{50}Au_{50}/C_3N_4$ and 50Pt + 50Au/C_3N_4, the absorption of the former was estimated to be about 0.9 times weaker from 420 to 1200 nm, but the H_2 evolution rate was ~one time higher. Interestingly, it is noticed that 50Pt + 50Au/C_3N_4 and 70Pt + 30Au/C_3N_4 samples exhibited higher activities than both Pt and Au samples, unlike what we found previously for the samples composed of mixed Au and Pt NPs loaded onto CeO_2 nanotubes for 4-nitrophenol reduction, where the catalytic reaction rate varied linearly with Pt/Au ratios between those of Au NPs/CeO_2 and Pt NPs/CeO_2. As mentioned above, Pt is one of the most efficient co-catalysts for water splitting with low overvoltage and fast kinetics. With increasing content of the Au NPs in the mixed samples, the plasmon absorption becomes stronger, and thus enhancing light absorption and hot electron injection into C_3N_4. These injected hot electrons may be directly used for catalysis or further transferred to nearby Pt NPs for catalysis on the Pt surface. But such an enhanced hot electron process, with increasing Au concentration, must be accompanied with the decrease of the number of the most efficient Pt NPs, since the overall metal loading is the same. The final catalytic performance is thus determined by the interplay of the enhanced, beneficial plasmonic effect and the negative effect due to the reduction of efficient Pt NPs in the system. The fact that 50Pt + 50Au/C_3N_4 and 70Pt + 30Au/C_3N_4 showed higher activity than Pt and Au samples underlines that in these two cases the plasmonic effect overrode the negative effect and became dominant. The 50Pt + 50Au/C_3N_4 sample yielded the highest activity among all the mixed samples and represented the optimal balance between the above mentioned effects in the mixed samples.

We tried to approximately estimate the respective contribution from the synergistic and plasmonic effects by focusing on the comparison of the reaction rate of the best alloy sample of $Pt_{50}Au_{50}/C_3N_4$, the mixture sample of 50Pt + 50Au/C_3N_4 and Pt/C_3N_4. It is reasonable to attribute the activity increase of 50Pt + 50Au/C_3N_4 with respect to Pt/C_3N_4 mainly to the plasmonic effect, which corresponded to be about 44% (31.0 vs 21.5 μmol h^{-1}). The impressive activity increase of ~ 200% (64.1 vs 21.5 μmol h^{-1}) of $Pt_{50}Au_{50}/C_3N_4$ could thus be largely due to

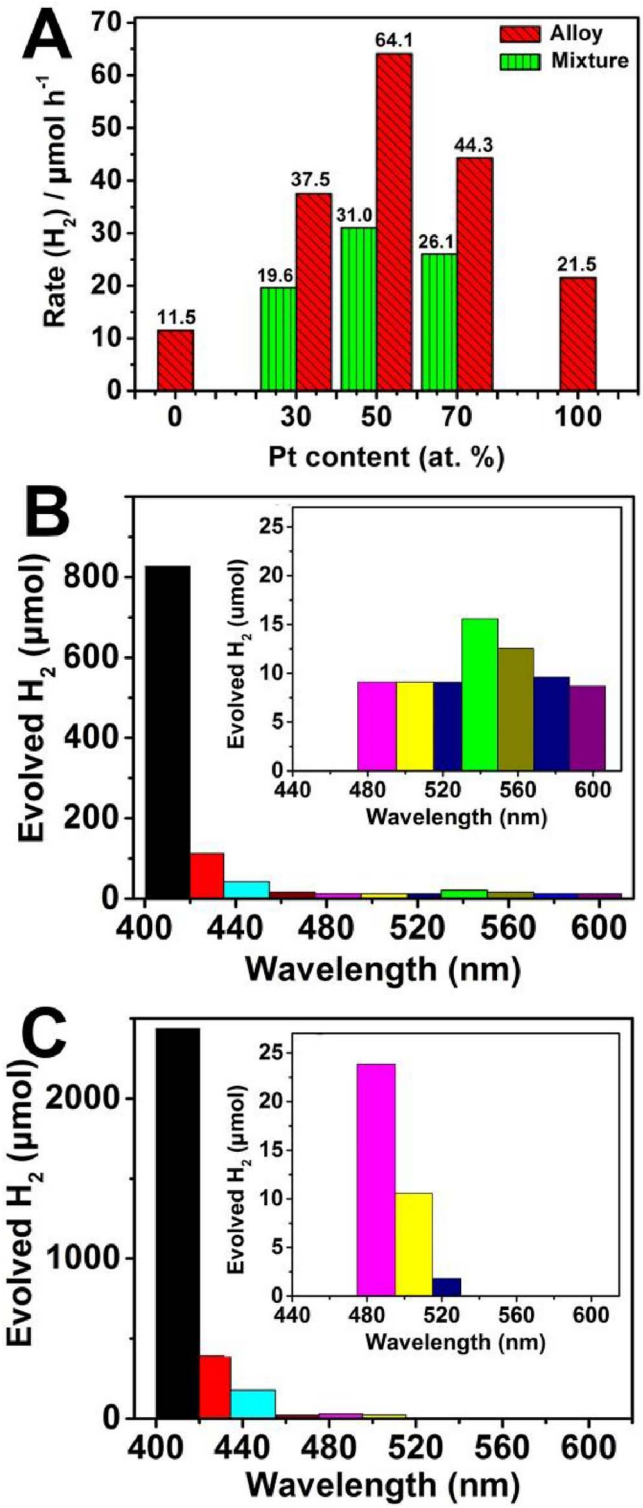

Fig. 4. (A) Variation of H_2 production rate with respect to the Pt content in alloy Pt_xAu_{100-x}/C_3N_4 and mixed xPt + (100-x)Au/C_3N_4, respectively (x = 100, 70, 50, 30, 0). Wavelength-dependent H_2 production of (B) 50Pt + 50Au/C_3N_4 and (C) $Pt_{50}Au_{50}/C_3N_4$. The insets of (B, C) show enlarged wavelength-dependent H_2 production at wavelengths longer than C_3N_4 absorption.

the beneficial synergistic effect, accounting for about ~156% activity increase. Such calculated synergistic contribution was actually even underestimated since the alloy sample absorbed much less photons then the mixture sample in the visible range. This analysis thus strongly indicates that the contribution from the synergistic effect is at least 3.5 times that of the plasmonic effect. The comparison was also made for other alloy samples. It was found that although the contribution from the syngergistic effect differed (2.2 times of the plasmonic effect for $Pt_{30}Au_{70}/C_3N_4$ and 3.9 times for $Pt_{70}Au_{30}/C_3N_4$), it was dominant in all the cases.

In order to straightforwardly observe the Au SPR effect on photocatalysis performance, we also measured the H_2 evolution rates of 50Pt + 50Au/C_3N_4 and $Pt_{50}Au_{50}/C_3N_4$ samples as a function of wavelengths by using a series of long-pass filters with cut-on wavelengths from 400 to 610 nm in combination with a 300W Xe lamp (Fig. S9, Supporting Information). In all testing the reaction temperature was stabilized at ~60 °C after 0.5 h and was not expected to affect the trend to be presented below. The evolution of H_2 at a specific wavelength range (λ_1–λ_2; $\lambda_1 < \lambda_2$) was estimated by subtracting H_2 generated with a λ_2 long-pass filter from that with a λ_1 long-pass filter after 2 h. It is clear that in general the H_2 evolution of both the 50Pt + 50Au/C_3N_4 and $Pt_{50}Au_{50}/C_3N_4$ samples decreased with increasing wavelength, suggesting the reaction depends on photoabsorption by photocatalysts (Fig. 4B, C). Closer examination of the data at longer wavelengths after removing data involving the strong contribution from C_3N_4, as shown in the insets, reveals that they have some obvious differences: 1) the wavelength ranges they reached the maximum H_2 generation were different. The 50Pt + 50Au/C_3N_4 sample showed the highest H_2 production with the irradiation between 530 and 550 nm (Fig. 4B inset), which was correlated very well with the Au SPR. Whereas the $Pt_{50}Au_{50}/C_3N_4$ sample showed the highest H_2 production in between 475 and 495 nm, in line with the highest intensity of the Xenon lamp around 475 nm (Fig. 4C inset); 2) the activity of the 50Pt + 50Au/C_3N_4 sample gradually decreased with wavelengths, extending to longer than 600 nm that corresponds to the broad plasmonic resonance, while the activity of the $Pt_{50}Au_{50}/C_3N_4$ sample quickly dropped to zero at a much shorter wavelength of ~530 nm. These wavelengths resolved results clearly demonstrate that the SPR excitation in the 50Pt + 50Au/C_3N_4 sample could provide additional enhancement for the H_2 production, although its contribution is much less as compared to the synergistic effect in the alloy samples. Even though the $Pt_{50}Au_{50}/C_3N_4$ sample also displayed the plasmonic absorption in the visible region, it is the synergistic effect that is the main and critical factor for the dramatically enhanced activity of this sample. With the same mass of noble metals, PtAu alloy NPs will definitely be a better choice in order to achieve higher catalysis performance.

We now comment on the relation between the optical and photocatalytic properties of the AuPt NPs. To understand this relation, our theoretical modeling in Fig. 1F will be very helpful. Our AuPt alloy NPs represent a very interesting class of plasmonic photocatalytic materials. They have both strong photocatalytic activity and the plasmon response; in the visible range. The enhanced overall photocatalysis of our AuPt NPs, with respect to pure Au and Pt NPs, mainly comes from the Pt component, which in its bulk form has the d-band close to the Fermi level and whose catalytic activity is further improved by its synergistic interactions with Au [45,46]. Simultaneously, the plasmon resonance is a key property of the Au-component, since pure Pt NPs have no plasmon resonance in the visible range. The plasmonic component (Au) is responsible for the enhanced optical absorption in our AuPt NPs via the plasmon resonance that leads to optical generation of excited electrons and holes in the Fermi gas in the visible range [21]. Then, these excited carriers contribute to the enhanced photocatalysis in the visible range. In this way, we take the advantages of both worlds, the photocatalytic materials (Pt) and the plasmonic materials (Au), by fabricating plasmonic, highly photocatalytic alloy NPs.

4. Conclusion

The synergistic effect in alloys and the plasmonic effect of plasmonic metals have been reported separately and considered as effective means for enhancing photocatalytic water splitting efficiency. It is now time to

compare their contributions to photocatalysis in similar systems in order to provide rational guides towards designing and realizing more efficient catalysts. In the current work, we deployed our investigations in this regard by constructing a complete comparative framework, a highly interesting nanocomposite system composed of C_3N_4, Pt, and Au nanocomponents. It was found that C_3N_4 anchored with PtAu alloy NPs demonstrated remarkably higher performance in H_2 evolution reaction in comparison with C_3N_4 anchored with Pt NPs, Au NPs, and the physical mixture of Pt and Au NPs at different ratios. Based on photocatalytic water splitting studies under different conditions and electrochemical testing, the strong synergistic effect between Pt and Au in alloy NPs was identified to be a dominant enhancement mechanism in this system and made significantly higher contribution to photocatalysis than that can be achieved by the plasmonic effect (maximized in the mixed samples). Theoretical calculations on plasmons of alloy NPs, based on the structural model derived from synchrotron measurements, using a simple effective-medium model reproduce the optical spectra of PtAu NPs very well and help with elaborating the relation between the optical and photocatalytic properties of the alloy NPs. This work represents the first systematic investigation and comparison of synergistic and plasmonic effects in similar systems and answers an important, yet not previously addressed question: synergistic and plasmonic effect, which can make more important contribution in a specific, promising catalysis system? It also provides guides for developing highly efficient photocatalysts in general. In particular, combination of plasmonic metal NPs with alloy NPs based on lower cost metals can be very promising.

Acknowledgements

Financial support from the Natural Sciences and Engineering Research Council of Canada (NSERC) in the context of NSERC-Discovery Grant and NSERC-Strategic Grant (with the support of Canadian Solar Inc.), Canada Research Chairs Program, and Fonds Quebecois sur la Recherche en Nature et Technologies are greatly appreciated. Dr Xu and Dr Gao acknowledges the National Natural Science Foundation of China (NSFC 51402198) and the Natural Science Foundation of Liaoning Province (201602592) for financial support. A.O.G. and L.B. were funded by the U.S. Army Research Office under Grant W911NF-12-1-0407, by Volkswagen Foundation (Germany). CLS@APS facilities (Sector 20-BM) at the Advanced Photon Source (APS) are supported by the U.S. Department of Energy (DOE), NSERC Canada, the University of Washington, the Canadian Light Source (CLS), and the APS. Use of the APS is supported by the DOE under Contract No. DE-AC02 − 06CH11357. The CLS is financially supported by NSERC Canada, CIHR, NRC, and the University of Saskatchewan.

Appendix A. Supplementary data

Supplementary data associated with this article can be found, in the online version, at http://dx.doi.org/10.1016/j.apcatb.2017.08.085.

References

[1] H. Li, Y. Gao, Y. Zhou, F. Fan, Q. Han, Q. Xu, X. Wang, M. Xiao, C. Li, Z. Zou, Nano Lett. 16 (2016) 5547–5552.
[2] M. Chen, J. Gu, C. Sun, Y. Zhao, R. Zhang, X. You, Q. Liu, W. Zhang, Y. Su, H. Su, D. Zhang, ACS Nano 10 (2016) 6693–6701.
[3] X. Liu, W. Di, W. Qin, Appl. Catal. B: Environ. 205 (2017) 158–164.
[4] N.S. Lewis, D.G. Nocera, Proc. Natl. Acad. Sci. 103 (2006) 15729–15735.
[5] M.P. Moloney, J. Govan, A. Loudon, M. Mukhina, Y.K. Gun'ko, Nat. Protoc. 10 (2015) 558–573.
[6] B. Luo, Y.C. Pu, S.A. Lindley, Y. Yang, L. Lu, Y. Li, X. Li, J.Z. Zhang, Angew. Chem. 128 (2016) 9010–9014.
[7] Y. Wang, H. Wang, F. Chen, F. Cao, X. Zhao, S. Meng, Y. Cui, Appl. Catal. B: Environ. 206 (2017) 417–425.
[8] M. Gratzel, Nature 414 (2001) 338–344.
[9] M.G. Walter, E.L. Warren, J.R. McKone, S.W. Boettcher, Q. Mi, E.A. Santori, N.S. Lewis, Chem. Rev. 110 (2010) 6446–6473.
[10] M.G. Kibria, H.P.T. Nguyen, K. Cui, S. Zhao, D. Liu, H. Guo, M.L. Trudeau, S. Paradis, A.-R. Hakima, Z. Mi, ACS Nano 7 (2013) 7886–7893.
[11] Y.H. Li, Y. Wang, L.R. Zheng, H.J. Zhao, H.G. Yang, C. Li, Appl. Catal. B: Environ. 209 (2017) 247–252.
[12] C. Zhu, C. Liu, Y. Zhou, Y. Fu, S. Guo, H. Li, S. Zhao, H. Huang, Y. Liu, Z. Kang, Appl. Catal. B: Environ. 216 (2017) 114–121.
[13] J. Liu, Y. Liu, N. Liu, Y. Han, X. Zhang, H. Huang, Y. Lifshitz, S.-T. Lee, J. Zhong, Z. Kang, Science 347 (2015) 970.
[14] J. Shi, Chem. Rev. 113 (2013) 2139–2181.
[15] M. Liu, W. Zhou, T. Wang, D. Wang, L. Liu, J. Ye, Chem. Commun. 52 (2016) 4694–4697.
[16] M.A.H. Muhammed, M. Döblinger, J. Rodríguez-Fernández, J. Am. Chem. Soc. 137 (2015) 11666–11677.
[17] M. Gao, P.K.N. Connor, G.W. Ho, Energy Environ. Sci. 9 (2016) 3151–3160.
[18] S.K. Cushing, J. Li, F. Meng, T.R. Senty, S. Suri, M. Zhi, M. Li, A.D. Bristow, N. Wu, J. Am. Chem. Soc. 134 (2012) 15033–15041.
[19] S. Linic, P. Christopher, D.B. Ingram, Nat. Mater. 10 (2011) 911–921.
[20] Z. Xu, M. Quintanilla, F. Vetrone, A.O. Govorov, M. Chaker, D. Ma, Adv. Funct. Mater. 25 (2015) 2950–2960.
[21] A.O. Govorov, H. Zhang, H.V. Demir, Y.K. Gun'ko, Nano Today 9 (2014) 85–101.
[22] Y. Tian, T. Tatsuma, J. Am. Chem. Soc. 127 (2005) 7632–7637.
[23] Z. Liu, W. Hou, P. Pavaskar, M. Aykol, S.B. Cronin, Nano Lett. 11 (2011) 1111–1116.
[24] S. Mubeen, J. Lee, N. Singh, S. Kramer, G.D. Stucky, M. Moskovits, Nat Nano 8 (2013) 247–251.
[25] S.K. Cushing, N. Wu, J. Phys. Chem Lett. (2016) 666–675.
[26] W. Fan, C. Chen, H. Bai, B. Luo, H. Shen, W. Shi, Appl. Catal. B: Environ. 195 (2016) 9–15.
[27] A.O. Govorov, H. Zhang, Y.K. Gun'ko, J. Phys. Chem. C 117 (2013) 16616–16631.
[28] Z. Xu, Y. Liu, F. Ren, F. Yang, D. Ma, Coord. Chem. Rev. 320–321 (2016) 153–180.
[29] P.N. Duchesne, P. Zhang, Nanoscale 4 (2012) 4199–4205.
[30] J.A. Lopez-Sanchez, N. Dimitratos, C. Hammond, G.L. Brett, L. Kesavan, S. White, P. Miedziak, R. Tiruvalam, R.L. Jenkins, A.F. Carley, D. Knight, C.J. Kiely, G.J. Hutchings, Nat. Chem. 3 (2011) 551–556.
[31] J. Zhang, D.N. Oko, S. Garbarino, R. Imbeault, M. Chaker, A.C. Tavares, D. Guay, D. Ma, J. Phys. Chem. C 116 (2012) 13413–13420.
[32] J. Zhang, G. Chen, M. Chaker, F. Rosei, D. Ma, Appl. Catal. B: Environ. 132 (2013) 107–115.
[33] J. Zhang, G. Chen, M. Chaker, F. Rosei, D. Ma, Appl. Catal. B 132–133 (2013) 107–115.
[34] S. Li, J. Zhang, M.G. Kibria, Z. Mi, M. Chaker, D. Ma, R. Nechache, F. Rosei, Chem. Commun. 49 (2013) 5856–5858.
[35] J. Zhang, G. Chen, D. Guay, M. Chaker, D. Ma, Nanoscale 6 (2014) 2125–2130.
[36] T. Ressler, J. Synchrotron Radiat. 5 (1998) 118–122.
[37] A.L. Ankudinov, B. Ravel, J.J. Rehr, S.D. Conradson, Phys. Rev. B 58 (1998) 7565–7576.
[38] Q. Jiang, L.H. Liang, D.S. Zhao, J. Phys. Chem. B 105 (2001) 6275–6277.
[39] A.R. Denton, N.W. Ashcroft, Phys. Rev. A 43 (1991) 3161–3164.
[40] X. Wang, K. Maeda, A. Thomas, K. Takanabe, G. Xin, J.M. Carlsson, K. Domen, M. Antonietti, Nat. Mater. 8 (2009) 76–80.
[41] Y. Hou, A.B. Laursen, J. Zhang, G. Zhang, Y. Zhu, X. Wang, S. Dahl, I. Chorkendorff, Angew. Chem. Int. Ed. 52 (2013) 3621–3625.
[42] Y. Yang, Y. Guo, F. Liu, X. Yuan, Y. Guo, S. Zhang, W. Guo, M. Huo, Appl. Catal. B: Environ. 142–143 (2013) 828–837.
[43] K. Maeda, X. Wang, Y. Nishihara, D. Lu, M. Antonietti, K. Domen, J. Phys. Chem. C 113 (2009) 4940–4947.
[44] R. Su, R. Tiruvalam, A.J. Logsdail, Q. He, C.A. Downing, M.T. Jensen, N. Dimitratos, L. Kesavan, P.P. Wells, R. Bechstein, H.H. Jensen, S. Wendt, C.R.A. Catlow, C.J. Kiely, G.J. Hutchings, F. Besenbacher, ACS Nano 8 (2014) 3490–3497.
[45] A. Ruban, B. Hammer, P. Stoltze, H.L. Skriver, J.K. Nørskov, J. Mol. Catal. A: Chem. 115 (1997) 421–429.
[46] B. Hammer, J.K. Nørskov, Advances in Catalysis, Academic Press, 2000, pp. 71–129.